Plasma Sources Science and Technology

ACCEPTED MANUSCRIPT

Magnetized fluid electron model within a two-dimensional hybrid simulation code for electrodeless plasma thrusters

To cite this article before publication: Jiewei Zhou *et al* 2022 *Plasma Sources Sci. Technol.* in press https://doi.org/10.1088/1361-6595/ac64bc

Magnetized fluid electron model within a two-dimensional hybrid simulation code for electrodeless plasma thrusters

J. Zhou, A. Domínguez-Vázquez, P. Fajardo and E. Ahedo

Equipo de Propulsión Espacial y Plasmas (EP2), Universidad Carlos III de Madrid, Leganés, Spain

Email: jzhou@pa.uc3m.es

Abstract

An axisymmetric fluid model for weakly-collisional, magnetized electrons is introduced and coupled to a particle-in-cell model for heavy species to simulate electrodeless plasma thrusters. The numerical treatment of the model is based on a semi-implicit time scheme, and specific algorithms for solving on a magnetic field aligned mesh. Simulation results of the plasma transport are obtained for a virtual electrodeless thruster. The particle and energy fluxes of electrons are discussed. A first phenomenological model is included for the anomalous cross-field electron transport, and a second one for the anomalous parallel-field electron cooling in the plume. The balances of the plasma properties reveal that wall losses are the crucial reason for the poor thrust efficiency of these thrusters. The magnetic thrust inside the source could be negative and largely depending on the location of the magnetic throat, which is found uncoupled from the location of the plasma beam sonic surface. Furthermore, a sensitivity analysis of the results against the simulated plume extension shows that finite plumes imply an incomplete electron expansion, which leads to underestimating the performances.

1 Introduction

The electrodeless plasma thruster (EPT) is a novel electric propulsion (EP) concept, in which plasma production and heating is achieved by an absorption of electromagnetic (EM) power, and a magnetic nozzle (MN) is used for plasma acceleration [1]. In an EPT, the propellant injected into a cylindrical vessel is ionized by the electrons, which interact with the EM waves emitted from an internal or external 'antenna'. The resulting current-free plasma is guided by the stationary applied magnetic field created by a set of coils or magnets. Inside the vessel, the magnetic field confines the plasma and allows the penetration of the EM waves; quasiaxial magnetic topologies are common but not unique. Outside the vessel, the magnetic field is divergent and acts as a MN that (i) expands the plasma and transforms its thermal energy into quasiaxial kinetic energy, and (ii) generates magnetic thrust. Two main realizations of the EPT concept are the electron cyclotron resonance thruster (ECRT) [2, 3], and the helicon plasma thruster (HPT) [4, 5, 6, 7]. The main differences between both concepts are the EM wave type and the mechanism for power absorption. In the ECRT, it is based on the electron cyclotron resonance, wave frequencies are within the microwave GHz range, and magnetic strengths are in the 1000-Gauss range. In the HPT, it depends on the propagation of helicon and Trivelpiece-Gould waves within the plasma column, wave frequencies and magnetic strengths are typically within the 10-MHz range and the 100-1000 Gauss range, respectively.

EPTs are technologies under extensive research with potential advantages over mature ones in some aspects. The electrodes, typical of the mature ones, are eliminated avoiding associated life-limiting constraints and contamination issues, and also allowing an ampler choice of propellants. Furthermore, EPTs do not need neutralizers, making simpler the whole thruster system including the usually expensive power control unit. Finally, EPTs offer high operation throttlability for a given power, and even magnetic thrust steering [8, 9]. However, most EPT prototypes still report thrust efficiencies lower than 10% [7, 10, 11, 12]. In order to continue that research, understanding the plasma physics in these devices is certainly a central task.

The plasma discharge in EPTs has two distinguished processes: plasma-wave interaction and plasma transport, which, although coupled, require their own models. This work is focused on modeling the 2D axisymmetric plasma transport. Fruchtman et al [13] were the first to develop, for an EPT source with an axial magnetic field, a variable-separation, 2D fluid model (a method which had been successfully applied previously to Hall thruster discharges [14]). Ahedo and Navarro [15] extended that development to the plasma plume applying the divergent MN model of Ahedo and Merino [16], and carried out extensive parametric and performance studies revealing, for instance, the large plasma losses in the thruster back wall (due to the lack of magnetic confinement), and those caused by multiple re-ionization (due to the wall recombination). Some important simplifications of these models are: the null radial component of the magnetic field inside the source; the arbitrary imposition of local current ambipolarity inside the source (not in the plume); the sonic flow transition anchored to the thruster exit; the fully collisionless plume with fully magnetized electrons; the use of a constant electron temperature map to avoid solving the electron energy equation.

In this work, a 2D hybrid model over a generic magnetic field configuration is adopted. The model releases all the constraints mentioned above and additionally provides a kinetic representation of the heavy species. The model consists of a particle-in-cell (PIC) model with Monte Carlo collisions for heavy species and a magnetized, diffusive fluid model for the electrons. Axisymmetric hybrid formulations are a good option to analyze the plasma discharge and performances of EPTs and Hall effect thrusters (HETs), since they offer a good trade-off between physical accuracy and simulation cost [17, 18]. The PIC model is appropriate for the rarefied conditions of the plasma, while the electron fluid model avoids huge computational costs, typical of electron kinetic formulations. Besides, quasineutrality is easily implemented in hybrid models and non-neutral effects are limited to Debye sheaths, which are treated as electrostatic discontinuities around the thruster walls. One limitation of axisymmetric hybrid models, however, is that they continue to be unable to reproduce the electron cross-field transport due to azimuthal instabilities [19, 20, 21, 22].

The hybrid model is implemented numerically in the code HYPHEN [23, 24, 25]. The PIC model of HYPHEN is inherited from the works of Fife, Parra and coworkers for the HET hybrid codes HPHALL [17] and HPHALL-2 [18]. The electron fluid model for HYPHEN is fully 2D and relies on the use of a magnetic field aligned mesh (MFAM) to avoid numerical diffusion caused by strong magnetic anisotropy [26, 27]. A first implementation of the electron model in an MFAM was done by Pérez-Grande, based mainly on Weighted Least Square Method (WLSM) numerical algorithms. Zhou et al [27] realized that the accuracy of these algorithms in the highly-irregular MFAM was insufficient often; developed better algorithms for both inner cells, based on Finite Difference Methods (FDMs), and boundary cells (based on improved WLSMs); and did the implementation for a simplified polytropic electron model. For the present work, these algorithms have been extended for the electron energy equation.

There are experimental evidences of plume cooling in EPTs (also in HETs and other thrusters) [28, 29, 30, 31], which cannot be explained by the weak collisionality of the plasma and is not reproduced by the commonly-used Fourier's (conductive) tensor law for the heat flux [18, 26]. Indeed, kinetic studies with paraxial MNs [32, 33] show that, in plumes, the heat flux is approximately proportional to the

enthalpy flux (i.e. it has a convective character). In addition, mixed (convective/conductive) heat flux closures have been proposed for mild collisionality regimes [34]. The extension of these kinetic studies to 2D and 3D magnetized scenarios is little known yet. In this work, with the purpose of matching trends observed in experiments and kinetic studies, a Fourier's law is used with a thermal conductivity tensor bearing anomalous terms both in the directions perpendicular and parallel to the magnetic field.

The axisymmetric hybrid model will be tested and applied to a virtual EPT, which has a design typical of real prototypes. Full 2D maps of main plasma magnitudes will be discussed with emphasis on electron-related magnitudes such as the electron current density, the electron temperature, the electron magnetic force, and the plasma properties on walls. The failure of the local current ambipolarity in the MN will be highlighted too. To end, the analysis of performances will allow to understand, for EPTs, the main phenomena degrading the overall efficiency.

The rest of the paper is organized as follows. Section 2 describes the generalities of HYPHEN, and the electron fluid model. Section 3 discusses the nominal simulation results for the EPT. Section 4 discusses further insights of the results. Section 5 summarizes the conclusions.

2 Hybrid model of plasma transport

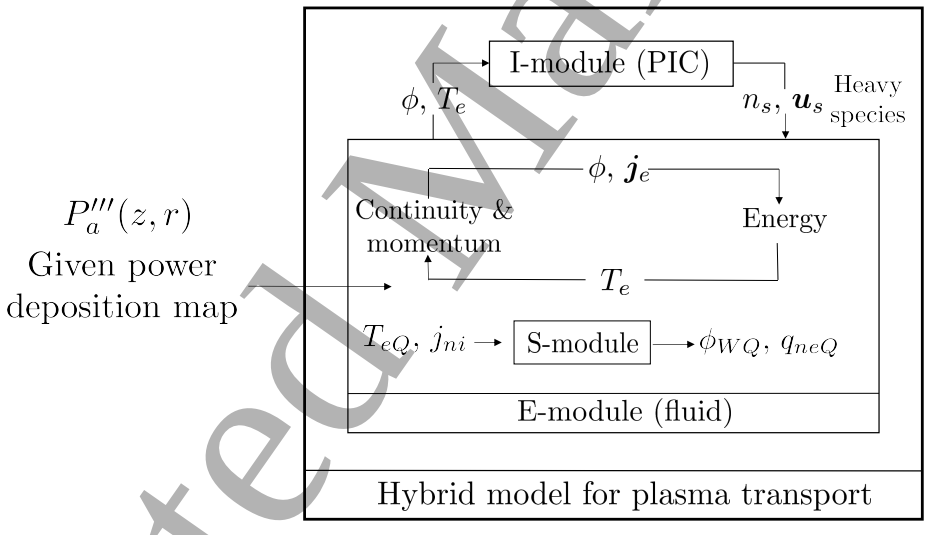

Figure 1: Structure of the modules and inputs/outputs for the simulation code.

2.1 Generalities

Figure 1 illustrates the modular structure of the hybrid code HYPHEN. For application to EPTs, the plasma discharge is organized in four models, each one constituting a core module. The modules are run sequentially and share input and output maps of several plasma variables. There is, first, the wave(W)-module, which solves the Maxwell equations for penetration of the high-frequency EM waves within the plasma column [35, 36]. Then, there are the ion(I)- and electron(E)-modules solving the slow (or quasisteady) plasma transport. The I-module implements the PIC model for heavy species, and the E-module the fluid model for electrons. The sheath(S)-module solves the Debye sheaths around the thruster walls.

The modules are run with a sequential time-marching method in a simulation loop. The I-module advances a time step Δt in an iteration, while the E-module includes an internal loop with a number of subiterations N_e and time step $\Delta t_e = \Delta t/N_e$. After a number of steps N_w of the transport modules, i.e. a time $N_w \Delta t$, the W-module is called for updating the power deposition map. Let us denote: Z_s, n_s, $\boldsymbol{u}_s$ and $\boldsymbol{j}_s = Z_s e n_s \boldsymbol{u}_s$ as, respectively, the charge number, the density, the velocity and the current density of species s (electrons e, ions i or neutrals n); ϕ the electric potential, T_e the electron temperature and $\boldsymbol{q}_e$ the electron heat flux; and P_a''' the local absorbed power density. This work does not simulate the EM antenna and the wave-plasma interaction process; instead, the W-module is bypassed and the stationary P_a'''-map is directly an input to the E-module. The other inputs of the E-module are the instantaneous properties of the heavy species.

The I-module uses a cartesian mesh defined on the cylindrical reference frame $\{\mathbf{1}_z,\ \mathbf{1}_r,\ \mathbf{1}_\theta\}$, with coordinates $(z,\ r,\ \theta)$. Figure 2 (a) shows the mesh, which is non-uniform and adapted to the expected gradients of plasma properties. The E-module uses a MFAM due the anisotropic character of the magnetized electron fluid. The applied magnetic field $\boldsymbol{B}$ defines the magnetic reference frame $\{\mathbf{1}_\parallel,\ \mathbf{1}_\perp,\ \mathbf{1}_\theta\}$, $\mathbf{1}_\parallel = \boldsymbol{B}/B$ and $\mathbf{1}_\perp = -\mathbf{1}_\parallel \times \mathbf{1}_\theta$, with coordinates $(\sigma,\ \lambda,\ \theta)$. The orthogonal coordinates $\lambda(z,r)$ and $\sigma(z,r)$ are obtained from the solenoidal and irrotational conditions, $\nabla \cdot \boldsymbol{B} = 0$ and $\nabla \times \boldsymbol{B} = 0$:

$$\frac{\partial \lambda}{\partial z} = -rB_r, \quad \frac{\partial \lambda}{\partial r} = rB_z, \tag{1}$$

$$\frac{\partial \sigma}{\partial z} = B_z, \quad \frac{\partial \sigma}{\partial r} = B_r. \tag{2}$$

Notice that λ isolines are streamlines while σ ones are equipotential lines. Figure 2 (b) shows the MFAM generated as result of λ and σ isolines intersection. The selection of the isolines is a complex process, since $\boldsymbol{B}$ is non-uniform in general, λ and σ are not either; Ref. [37] discusses the meshing strategies.

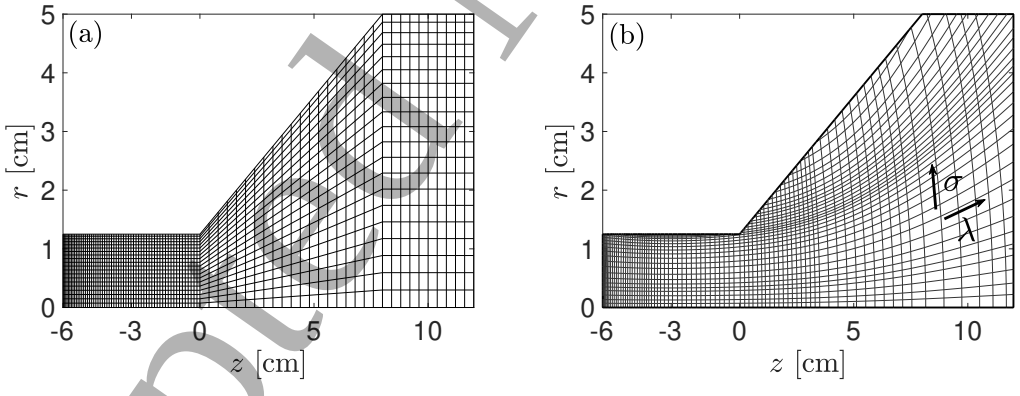

Figure 2: (a) Cartesian mesh of the I-module and (b) magnetic field aligned mesh of the E-module.

2.2 Electron fluid model

The drift-diffusive (inertialess), magnetized, weakly-collisional fluid model for electrons consists of the equations

$$n_e = \sum_{s \neq e} Z_s n_s, \tag{3}$$

$$\nabla \cdot \boldsymbol{j}_e = -\nabla \cdot \boldsymbol{j}_i \tag{4}$$

$$0 = -\nabla(n_e T_e) + e n_e \nabla\phi + \boldsymbol{j}_e \times \boldsymbol{B} + \boldsymbol{F}_{res} + \boldsymbol{F}_{ano}, \tag{5}$$

$$\frac{\partial}{\partial t}\left(\frac{3}{2} n_e T_e\right) + \nabla \cdot \left(\frac{5}{2} T_e n_e \boldsymbol{u}_e + \boldsymbol{q}_e\right) = -\nabla\phi \cdot \boldsymbol{j}_e + P_a''' - P_{inel}''', \tag{6}$$

$$0 = -\frac{5 n_e T_e}{2e} \nabla T_e - \boldsymbol{q}_e \times \boldsymbol{B} + \boldsymbol{Y}_{res} + \boldsymbol{Y}_{ano}, \tag{7}$$

and the unknowns are n_e, ϕ, $\boldsymbol{j}_e$, T_e and $\boldsymbol{q}_e$.

Equation (3) states the plasma quasineutrality and Eq. (4) is the conservation of electric current density $\boldsymbol{j} = \boldsymbol{j}_e + \boldsymbol{j}_i$, and the right sides of both equations are provided by the I-module. Notice that, thanks to plasma quasineutrality and the absence of volumetric sources of net current, Eq. (4) for the current conservation is much more convenient numerically than the electron continuity equation, $\partial n_e/\partial t + \nabla \cdot n_e \boldsymbol{u}_e = S_e$, where S_e is the source term of electrons. In the hybrid formulation followed here, S_e is computed by the I-module through the ionization events for both singly and doubly charged ions, as explained in previous works [17, 18, 38, 39]. Collision data comes from the BIAGI database [40] for single-ion generation, and the Drawin model [41] for double-ion generation.

In the momentum equation (5), all inertia terms are neglected, $\boldsymbol{F}_{ano}$ accounts for the anomalous cross-field transport, and $\boldsymbol{F}_{res}$ is the resistive force

$$\boldsymbol{F}_{res} = (m_e \nu_e / e)(\boldsymbol{j}_e + \boldsymbol{j}_c), \tag{8}$$

where $\nu_e = \sum_{s \neq e} \nu_{es}$ is the total momentum collision frequency of electrons, ν_{es} is the momentum collision frequency of electrons e with heavy species s, and $\boldsymbol{j}_c = e n_e \sum_{s \neq e} (\nu_{es}/\nu_e) \boldsymbol{u}_s$ is the contribution of heavy species to the resistive force.

Equation (6) is the electron energy conservation in the inertialess limit. On the left side, there are the flux of enthalpy and the heat flux; on the right side, there are the work of the electric field, the power deposition density P_a''', provided by the W-module, and the power losses from collisions

$$P_{inel}''' = n_e \sum_{s \neq e} \nu_{es,inel} \varepsilon_{es}, \tag{9}$$

where $\nu_{es,inel}$ and ε_{es} are, respectively, the collision frequency and energy threshold of inelastic collisions (e.g. ionization and excitation). In the heat flux equation (7), which has the same drift-diffusive character than the momentum equation (5), there is a resistive contribution

$$\boldsymbol{Y}_{res} = -(m_e \nu_e / e) \boldsymbol{q}_e, \tag{10}$$

and $\boldsymbol{Y}_{ano}$ accounts for anomalous effects.

Anomalous electron cross-field transport is likely due to saturated azimuthal instabilities. Since no established model exist for them, for electron momentum, the time and azimuth averaged effect on the axisymmetric discharge is included via the simple phenomenological model [18, 26]

$$\boldsymbol{F}_{ano} = \alpha_{ano} B j_{\theta e} \boldsymbol{1}_\theta, \tag{11}$$

with α_{ano} a fitting parameter measuring the average turbulence level. Regarding electron energy, it is

$$\boldsymbol{Y}_{ano} = -\alpha_{ano} B q_{\theta e} \boldsymbol{1}_\theta - (m_e \nu_q / e) q_{\parallel e} \boldsymbol{1}_\parallel, \tag{12}$$

and models two different effects. The first one is caused by the saturated azimuthal instabilities leading to anomalous (cross-field) transport, and the second one, with ν_q an empirical collisionality, accounts for anomalous (parallel-field) cooling in the near-collisionless plume [28, 32].

Solving the momentum equation for the components of $\boldsymbol{j}_e$ in the magnetic frame yields the generalized Ohm's law

$$j_{\parallel e} = \sigma_{\parallel e}\left[\frac{T_e}{e}\frac{\partial \ln n_e}{\partial \mathbf{1}_\parallel} + \frac{1}{e}\frac{\partial T_e}{\partial \mathbf{1}_\parallel} - \frac{\partial \phi}{\partial \mathbf{1}_\parallel}\right] - j_{\parallel c}, \tag{13}$$

$$j_{\perp e} = \sigma_{\perp e}\left[\frac{T_e}{e}\frac{\partial \ln n_e}{\partial \mathbf{1}_\perp} + \frac{1}{e}\frac{\partial T_e}{\partial \mathbf{1}_\perp} - \frac{\partial \phi}{\partial \mathbf{1}_\perp}\right] - \frac{j_{\perp c} - \chi_t j_{\theta c}}{1+\chi\chi_t}, \tag{14}$$

$$j_{\theta e} = \chi_t j_{\perp e} - \frac{\chi_t}{\chi} j_{\theta c}, \tag{15}$$

where

$$\chi = \frac{\omega_{ce}}{\nu_e}, \quad \chi_t = \frac{\omega_{ce}}{\nu_e + \alpha_{ano}\omega_{ce}}, \tag{16}$$

are the two Hall parameters of interest, with $\omega_{ce} = eB/m_e$; and

$$\sigma_{\parallel e} = \frac{e^2 n_e}{m_e \nu_e}, \qquad \sigma_{\perp e} = \frac{e^2 n_e}{m_e \nu_{\perp e}} \tag{17}$$

are the scalar conductivities, with $\nu_{\perp e} = \nu_e(1+\chi\chi_t)$.

By analogy to the Ohm's law, solving the heat flux equation for $\boldsymbol{q}_e$ yields the generalized Fourier's law

$$q_{\parallel e} = -K_{\parallel e}\frac{\partial T_e}{\partial \mathbf{1}_\parallel}, \tag{18}$$

$$q_{\perp e} = -K_{\perp e}\frac{\partial T_e}{\partial \mathbf{1}_\perp}, \tag{19}$$

$$q_{\theta e} = \chi_t q_{\perp e}, \tag{20}$$

with

$$K_{\parallel e} = \frac{5}{2}\frac{n_e T_e}{m_e \nu'_e}, \qquad K_{\perp e} = \frac{5}{2}\frac{n_e T_e}{m_e \nu_{\perp e}}, \tag{21}$$

scalar thermal conductivities, and $\nu'_e = \nu_e + \nu_q$ the effective collision frequency for parallel thermal transport.

The cross-field transport is significant for $\alpha_{ano}\omega_{ce} \geq \nu_e$: as α_{ano} increases, $\nu_{e\perp}$ decreases, and $\sigma_{\perp e}$ and $K_{\perp e}$ increase, which leads generally to increase both $j_{\perp e}$ and $q_{\perp e}$. In the Fourier's law for parallel transport (18), the large parallel conductivity (for $\nu_q = 0$) implies a negligible parallel temperature gradient, much smaller than experimental evidences, and the phenomenological parameter ν_q allows a fitting of that gradient. In the Ohm's law for parallel transport (13), the large parallel conductivity implies

$$\frac{\partial \phi}{\partial \mathbf{1}_\parallel} \approx \frac{T_e}{e}\frac{\partial \ln n_e}{\partial \mathbf{1}_\parallel} + \frac{1}{e}\frac{\partial T_e}{\partial \mathbf{1}_\parallel} \sim \frac{T_e}{e}\frac{\partial \ln n_e}{\partial \mathbf{1}_\parallel} \gg \frac{j_{\parallel e} + j_{\parallel c}}{\sigma_{\parallel e}}. \tag{22}$$

Thus, often the Boltzmann relation $\phi \propto (T_e/e)\ln n_e$ is approximately satisfied along magnetic lines and makes convenient the use of thermalized potential $\Phi = \phi - (T_e/e)\ln n_e$ instead of ϕ as unknown in the numerical equations [27].

At each boundary of the quasineutral domain, boundary conditions are imposed on $j_n = \boldsymbol{j}\cdot\boldsymbol{n}$ and $q_{ne} = \boldsymbol{q}_e \cdot \boldsymbol{n}$, with $\boldsymbol{n}$ the outward unit normal. On the axis, symmetry imposes that both fluxes are null. Appendix A provides expressions for them *at the sheath edges* of the thruster walls. For a current-free plasma beam, the integral of j_n along the whole plume boundary must be null, but local conditions at the plume boundary are complex to define. Here, we impose $j_n = 0$ and

$$q_{ne} = c_q T_e n_e u_{ne}, \tag{23}$$

with c_q a constant (we take $c_q = 2$ in the nominal simulation).

Finally, for the numerical integration, it is convenient to define the total energy flux vector

$$\boldsymbol{P}''_{\star e} = \boldsymbol{P}''_e - e\phi n_e \boldsymbol{u}_e, \tag{24}$$

adding the flux of potential energy to the electron enthalpy and heat fluxes $\boldsymbol{P}''_e = (5/2)T_e n_e \boldsymbol{u}_e + \boldsymbol{q}_e$ (in the present electron model, $(1/2)m_e u_e^2 n_e \boldsymbol{u}_e$ is assumed negligible). Then, the energy equation (6), can be expressed in a similar functional form as the current continuity equation (4),

$$\nabla \cdot \boldsymbol{P}''_{\star e} = -\frac{\partial}{\partial t}\left(\frac{3}{2} n_e T_e\right) - \phi \nabla \cdot \boldsymbol{j}_i + P'''_a - P'''_{inel}. \tag{25}$$

(Interestingly, this equation reduces to the conservation condition $\nabla \cdot \boldsymbol{P}''_{\star e} \simeq 0$, for the steady state and regions with negligible power deposition and collisions, which will be the situation in most of the plume.)

The numerical treatment of the equations for ϕ, $\boldsymbol{j}_e$, T_e, $\boldsymbol{P}''_{\star e}$, is explained in Appendix B. This treatment is based on a semi-implicit scheme for the time discretization and finite volume/gradient reconstruction methods for the spatial discretization.

3 Analysis of plasma profiles and performances

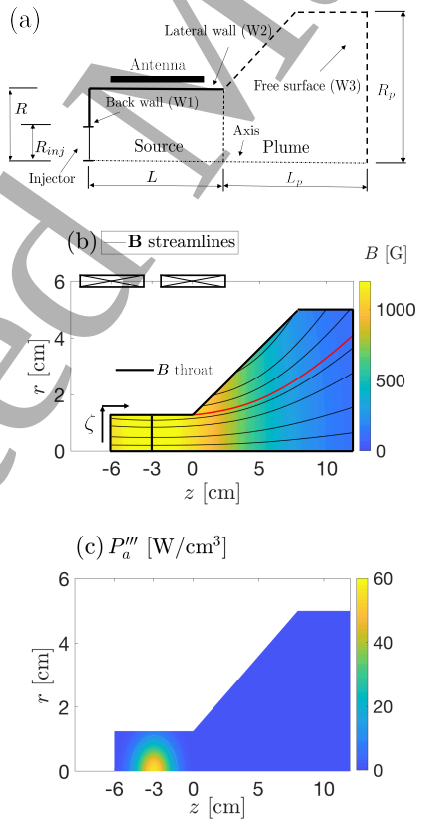

Figure 3: (a) Sketch of the EPT simulation domain. Input maps of (b) applied magnetic field (red line is the most external streamline line from the source) and (c) EM wave power deposition.

Figure 3 (a)-(c) sketches for the nominal simulation: the virtual EPT, which is similar to a prototype under research [7], the magnetic topology created by coils, and the power deposition map P_a'''. Table 1 summarizes the main simulation parameters. The thruster vessel is made of Boron Nitride, has a length $L = 6$cm and a radius $R = 1.25$cm. The injector, which is circular with a radius of $R_{inj} = 0.625$cm, is placed on the base of the vessel. The propellant is xenon, injected at the nominal case with a mass flow of $\dot{m} = 1$mg/s. The I-module considers neutrals, singly charged ions and doubly charged ions (although, in the nominal case, these ones are turned off).

The magnetic field is quasi-axial inside the source and divergent in the plume. The maximum strength is about 1200G, and the magnetic 'throat' is located at $z_t = -3$cm. The total power deposited in the plasma is $P_a = \int_{\Omega_p} P_a''' d\Omega = 300$W, with the integration over the whole simulation domain Ω_p and a Gaussian deposition map in (z, r) for P_a'''. The nominal parameters for anomalous transport and anomalous cooling are $\alpha_{ano} = 0.02$ and $\nu_q = 10^9 \mathrm{s}^{-1}$, respectively.

The simulation domain is bounded by the thruster back wall W1 and lateral wall W2, and the downstream free-loss surface W3. The plume, with a conical shape, has a length $L_p = 12$cm, and a maximum radius $R_p = 5$cm. Regarding the numerical settings, the meshes used by the I- and E-modules [Fig. 2] have, respectively, 1800 and 1961 cells. The time step used for ions is $\Delta t = 2.5 \cdot 10^{-8}$s, and the number of subiterations for electrons is $N_e = 10$. The results shown correspond to the steady state, obtained after running a simulation time of 2.5ms.

Simulation parameter	**Symbol**	**Units**	**Value**
Thruster length	L	cm	6
Thruster radius	R	cm	1.25
Injector radius	R_{inj}	cm	0.625
Mass flow	$\dot{m}$	mg/s	1
Simulated heavy species	-	-	Neutrals/Singly charged ions
Maximum magnetic strength	-	G	1200
Magnetic throat location	z_t	cm	-3
Total power deposited	P_a	W	300
Power deposition profile	-	-	Gaussian
Anomalous transport coefficient	α_{ano}	-	0.02
Anomalous cooling collisionality	ν_q	s^{-1}	10^9
Plume length	L_p	cm	12
Maximum plume radius	R_p	cm	5
I-mesh size	-	cells	1800
E-mesh size	-	cells	1961
I-module time step	Δt	s	$2.5 \cdot 10^{-8}$
E-module time subiterations	N_e	-	10
Total simulation time	-	ms	2.5
Density	n_e	m^{-3}	10^{16}-10^{20}
Temperature	T_e	eV	7-14
Collision frequency	ν_e	s^{-1}	10^6-10^7
Gyrofrequency	ω_{ce}	s^{-1}	10^9-10^{10}

Table 1: Nominal simulation parameters and typical electron conditions.

3.1 2D plasma profiles

Figure 4 illustrates the 2D maps of relevant plasma magnitudes. The outputs from the I-module are panels (a), (b) and (e). The other panels are obtained from the E-module. For any vector magnitude, say $\mathbf{\Gamma}$, it is going to be useful to distinguish (with a tilde) the longitudinal vector component $\tilde{\mathbf{\Gamma}} = \mathbf{\Gamma} - \Gamma_\theta \mathbf{1}_\theta$ from the azimuthal one.

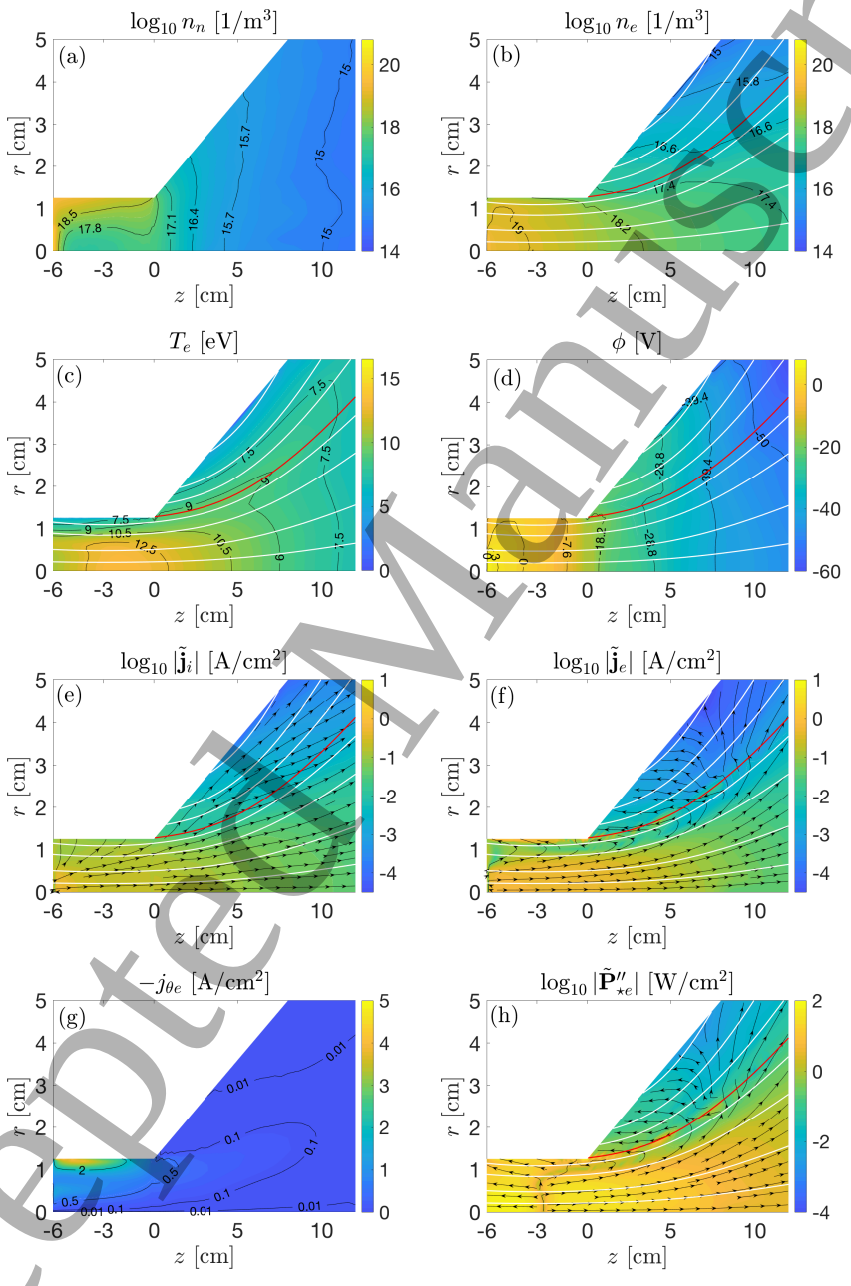

Figure 4: 2D maps of plasma magnitudes for the nominal simulation. Some plots show the magnetic field lines (white lines), and species streamlines (black arrows).

The neutral density [panel (a)] peaks at $n_n \approx 10^{20}\mathrm{m}^{-3}$ near the injector. Then, it falls 2 orders of magnitude due to ionization. Large neutral densities near the walls are due to ion recombination there.

These neutrals are ionized again, explaining their depletion near the axis; this effect is less noticeable near the vessel exit since the ionization rate is lower there. The ionization of injected neutrals makes the plasma density [panel (b)] to reach a maximum of $n_e \approx 5 \cdot 10^{19}\mathrm{m}^{-3}$ near the back wall. The radial decay of n_e inside the vessel is due to recombination; outside the vessel, n_e decays due to the plasma beam expansion and acceleration.

The electron temperature [panel (c)] is in the range T_e = 7-14eV. The maximum is near the vessel center, where the power deposition map peaks (Fig. 3 (c)). In the directions parallel and perpendicular to the magnetic field, the cooling is regulated by, respectively, the thermal conductivities $K_\parallel$ and $K_\perp$. Both of them contain anomalous terms, and the sensitivity to these parameters will be discussed later. The electric potential [panel (d)] presents a maximum near the back wall, which is close to the plasma density one. To the back wall, there is a small potential drop allowing the backflow of ions required by plasma quasineutrality. From source to far plume, the potential drop is $\Delta\phi \sim 50$V, about 3 times the maximum temperature $T_{e,max}$. Kinetic studies for MNs [32], supported by experiments [42], show that the ratio $e\Delta\phi/T_{e,max}$ depends on the propellant atomic mass, and here the results for xenon are consistent. The potential and density drops *along* the magnetic field lines follows approximately the Boltzmann relation, according again to models [15, 16] and experiments [43]. Inside the vessel, the electric potential is rather flat radially, a behavior typical of cylindrical plasmas confined by axial magnetic fields [15, 44]. In the plume top left side, near $(z, r) = (3, 2.5)$cm, there is even a local maximum of ϕ to enhance the transport of electrons towards this magnetically isolated region.

The map of $\tilde{\boldsymbol{j}}_i$ [panel (e)] shows that the ion motion is governed by the electric field. In the source, it does not allow to appreciate the ion backflow region, given the resolution, but it depicts well the ion flow to the lateral wall causing recombination. In the plume, the near-unmagnetized ions detach inwardly from the magnetic lines as expected [45]. The map of $\tilde{\boldsymbol{j}}_e$ [panel (f)] shows that electrons are attached to the magnetic lines except for high radii due to effects of boundary. The sum of the two currents yields the longitudinal net current, which, in general, is not null locally. Thus, local current ambipolarity is not fulfilled, even if the whole plasma beam is current-free; this was well known for the plume [27, 46] but less investigated for the source.

The electron azimuthal current [panel (g)] is, basically, the plasma azimuthal current, since the contributions of the near-unmagnetized ions is negligible (below 1%). The electron azimuthal current is diamagnetic, i.e. opposite to the azimuthal current of the coils [16, 47]. From the electron momentum equations (14) and (15), $j_{\theta e}$ contains contributions from electric field and pressure gradient drifts, and the latter is the dominant one.

Finally, the map of $\tilde{\boldsymbol{P}}''_{\star e}$ [panel (h)] is compared with the one of $\tilde{\boldsymbol{j}}_e$. In the source, they behave differently since the related source terms are different. However, in the near-collisionless, stationary plume, the 2D maps are similar and the two magnitudes decrease downstream due to the divergence of the beam. Further analysis for the main plume shows that (i) both $\tilde{\boldsymbol{q}}_e$ and $\tilde{\boldsymbol{j}}_e$ are almost parallel to the magnetic lines, and (ii) $q_{\parallel e} \approx \mathcal{E}_q n_e u_{\parallel e}$ with $\mathcal{E}_q \sim$ 10-20eV. As result, $-e\phi + (5/2)T_e + \mathcal{E}_q$ is approximately constant along magnetic lines of the main plume.

3.2 Particle and energy wall fluxes

Figure 5 (a) shows the fluxes (in units of currents) of plasma species *to* the thruster walls versus an arclength variable ζ (defined in Fig. 3), which starts at the center of the back wall W1 and covers until the lateral wall W2. The fluxes *from* the walls are not included.

The ion flux to the walls is recombined into neutrals. The magnetic topology attempts to shield W2 but not W1: the ion current is 0.1-1A/cm^2 at W1, and decays an order of magnitude at W2. The secondary electron emission yield of the dielectric walls is $\delta_{ws} \approx$ 0.2-0.4, and thus, the flux of secondary

electrons from the walls (representing the difference between the primary electron and ion currents in the plot) is $\delta_{ws}/(1-\delta_{ws}) \approx 0.2$-$0.6$ times the ion flux. The fluxes of the neutrals to the walls are much lower due to their low velocity. Aside from the injector, where the flux of propellant from the wall is of the order 0.1A/cm^2 (equivalent current), in the dielectric walls that flux is the sum of the ion and neutral fluxes to the walls.

Figure 5 (b) shows the mean impact energy of plasma species to the walls, i.e. ratio between the energy and the particle incoming fluxes. For hot primary electrons, the average impact energy is about $2T_e$ according to the sheath model. For cold ions, the impact energy is mainly kinetic, amounting to 15-35eV, with a contribution from the acceleration through the Debye sheath. In terms of erosion, a threshold of the impact energy is necessary for the sputtering, usually in the range 30-70eV for common ceramic materials in EP [48]. Thus, W1 is more prone to erosion due to its higher impact energy and fluxes. The average energy of impacting neutrals (about 2eV) are mainly due to neutrals from ion recombination, which are of low energy due to the wall accommodation.

The energy fluxes, obtained from multiplying the curves of Figs. 5 (a)-(b), are of interest for the thermal analysis of the thruster. Since the impact energies are homogeneous, these fluxes are found with similar shapes to the particle ones: 1-10W/cm^2 at W1 and an order of magnitude lower at W2.

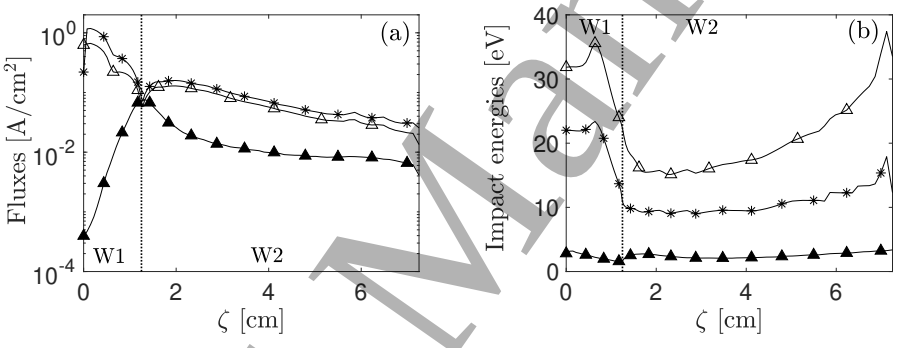

Figure 5: (a) Current densities to the thruster walls W1 and W2 (separated with a vertical dot line), and (b) mean impact energies per electron ($*$), ion ($\triangle$) and neutral ($\blacktriangle$). For neutrals, 1 ampere-equivalent (Aeq) of flux is $(1.6 \cdot 10^{-19})^{-1} \simeq 6.25 \cdot 10^{18}$ particles per second.

3.3 Propulsive performances

Appendix C presents the definitions of mass and energy flows at different surfaces, and the thrust obtained summing the contributions of the different species according to the PIC or fluid model used for them. The ion mass flow balance in steady state can be expressed as

$$\dot{m}_{i,total} = \dot{m}_{i,beam} + \dot{m}_{i,wall}, \tag{26}$$

where: $\dot{m}_{i,total}$ is the total ion volumetric production, $\dot{m}_{i,beam} = \dot{m}_{i,W3}$ is the ion beam mass flow downstream, and $\dot{m}_{i,wall} = \dot{m}_{i,W1} + \dot{m}_{i,W2}$ is the ion mass flow losses (via wall recombination) to the thruster walls. This leads to define the propellant utilization efficiency and production efficiency as

$$\eta_u = \frac{\dot{m}_{i,beam}}{\dot{m}}, \quad \eta_{prod} = \frac{\dot{m}_{i,beam}}{\dot{m}_{i,total}}. \tag{27}$$

For the nominal simulation, $\eta_u \simeq 96\%$ and $\eta_{prod} \simeq 14\%$ (see Table 2), so near full ionization is achieved but at the high cost of multiple ionizations. On average, a neutral is ionized more than 6 times due

to recombination, which is significant in the back and lateral walls with relative shares of 1/3 and 2/3, respectively. Since the area ratio between both walls is about 10, it is clear the penalty on the back wall.

The plasma power balance, in steady state, can be expressed as

$$P_a = P_{beam} + P_{wall} + P_{inel}, \tag{28}$$

with $P_{beam} = P_{W3}$, $P_{wall} = P_{W1} + P_{W2}$, and $P_{inel} = \int_{\Omega_p} P'''_{inel} d\Omega$. Power-related efficiencies of interest are the energy efficiency, the divergence efficiency and the dispersion efficiency, which are defined, respectively, as

$$\eta_{ene} = \frac{P_{beam}}{P_a}, \qquad \eta_{div} = \frac{P^{(z)}_{beam}}{P_{beam}}, \qquad \eta_{disp} = \frac{F^2}{2\dot{m} P^{(z)}_{beam}}. \tag{29}$$

Here, $P^{(z)}_{beam}$ is the flow of *axial* energy of the plasma. Notice that F, P_{beam} and $P^{(z)}_{beam}$ include the contributions of heavy species and electrons. Since electrons are not cold in this finite plume, they keep a residual momentum and energy. The contributions of electrons to these magnitudes are 5%, 40% and 26%, respectively.

The meaning of η_{ene} is evident. For the nominal simulation it is $\eta_{ene} \simeq 17.8\%$ since the large losses of both P_{wall} and P_{inel}, which are caused by multiple recombination and ionization. The divergence efficiency gives a measure of the plume radial divergence, based on axial and non-axial energies of the beam (notice that other authors use particle fluxes intead of energy fluxes). The value $\eta_{div} = 73.9\%$ is reasonable, corresponding to an average beam divergence angle of $\arccos\sqrt{\eta_{div}} \simeq 30$ deg. The dispersion efficiency measures the velocity dispersion of the beam population and would be 100% for a monoenergetic beam. The value $\eta_{disp} = 73.7\%$ implies that the ratio between the mean exhaust velocity, $F/\dot{m}$, and the ideal monoenergetic velocity, $(2P^{(z)}_{beam}/\dot{m})^{1/2}$, is $\sqrt{\eta_{disp}} \simeq 86\%$. The plume efficiencies are dependent on the residual electron energy and they increase as this energy vanishes, as we will show later.

The thrust efficiency is defined and factorized as

$$\eta_F = \frac{F^2}{2\dot{m} P_a} = \eta_{ene}\eta_{div}\eta_{disp}. \tag{30}$$

For the nominal simulation, it is 9.7%, well aligned with typical values measured in different EPTs [7, 10, 11, 12]. The factorization shows clearly that the issue is the poor η_{ene}, i.e. the bad magnetic confinement of the plasma inside the source, which is absent at the back wall, and seems reduced, because of the anomalous cross-field transport, at the lateral wall.

The nominal simulation has been run turning off the production of doubly charged ions. Table 2 compares the performances for this case and the one where doubly charged ions, coming from ionization of neutrals or singly charged ions, are considered. The production of doubly charged ions leads to little changes in the plasma maps. There is a mild increase of P_{inel}/P_a, a resultant mild decrease of T_e to 5-12eV and, then, of P_{wall}/P_a. Finally, F and η_F increase by 9% and 18%, respectively, which have some importance. Nonetheless, for the sake of simplicity and computational cost (about 3 days of simulation run time for the nominal case, and 6 days after including doubly charged ions), the rest of simulations presented next do not include doubly charged ions.

Case	F [mN]	η_F	η_{ene}	η_{div}	η_{disp}	η_u	η_{prod}	P_{wall}/P_a	P_{inel}/P_a
Nominal	7.64	0.097	0.178	0.74	0.74	0.96	0.14	0.482	0.340
Doubly charged ions	8.32	0.115	0.204	0.76	0.74	0.96	0.16	0.438	0.358
α_{ano}=0.01	9.32	0.144	0.263	0.74	0.74	0.98	0.24	0.549	0.188
ν_q=0	7.53	0.094	0.193	0.70	0.70	0.95	0.15	0.473	0.334
ν_q=10^{10}s^{-1}	8.51	0.120	0.176	0.83	0.82	0.96	0.13	0.466	0.358
Double plume	8.69	0.126	0.178	0.85	0.83	0.96	0.14	0.482	0.340

Table 2: Performances for several simulation cases.

3.4 Contributions to the total thrust

One of the main thrust mechanisms in EPTs comes from the diamagnetic azimuthal plasma currents [16, 49]. The magnetic circuit exerts on the plasma the force $\boldsymbol{j} \times \boldsymbol{B}$, with axial component $-j_\theta B_r$, and the plasma reacts with the same opposite force, which constitutes the magnetic thrust. For studying this mechanism, 3 magnetic configurations are considered with different axial positions with respect to the thruster (the currents of the coils are the same). They are characterized by the location of the MN throat: in the case $z_t = -6$cm, the throat is at the back of the vessel and the MN is divergent in the whole domain (typical of ECRTs [2, 3]); in the case $z_t = 0$cm, the throat is at the exit of the vessel and the MN is divergent in the plume only; the nominal simulation is the in-between case with $z_t = -3$cm.

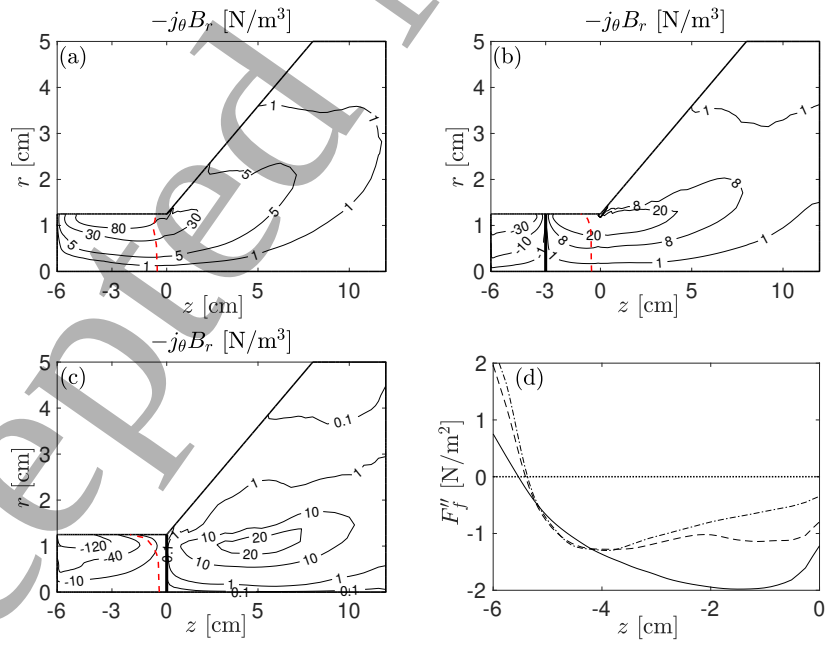

Figure 6: 2D maps of magnetic force density for 3 magnetic configurations with axial locations of the MN throat (vertical thick line) at (a) $z_t = -6$cm, (b) -3cm and (c) 0cm. (d) Friction force density at thruster lateral wall for $z_t = -6$cm (——), -3cm (- - - -) and 0cm (-.-.-.-).

z_t [cm]	F [mN]	F_p [mN]	F_f [mN]	F_m [mN]	$F_{m,s}$ [mN]	$F_{m,p}$ [mN]	$F_{m,c}$ [mN]	$F_{m,d}$ [mN]
-6	7.15	9.94	-5.97	3.18	1.60	1.58	0.00	3.18
-3	7.64	9.79	-3.63	1.48	-0.22	1.70	-0.54	2.02
0	6.69	9.30	-2.27	-0.34	-1.74	1.40	-1.74	1.40

Table 3: Contributions to the total thrust for 3 magnetic configurations with different axial locations of the MN throat.

Figures 6 (a)-(c) illustrates the 2D maps of the magnetic thrust density for the 3 configurations. Since B_r changes the sign at the MN throat, while $j_\theta > 0$ in the whole domain, the magnetic force density is negative in the convergent MN and positive in the divergent MN. Furthermore, since the plasma is denser inside the vessel, the negative force density in the convergent MN could be larger than the positive one and affect much the net magnetic thrust. The ion flow sonic surface (shown as red lines) is almost invariant for the 3 configurations, and located near the thruster exit at $z \approx -0.6$cm. The main difference among the 3 cases is next to the wall, due to the different momentum loss of heavy particles impacting the wall. Thus, the ion sonic surface is more related to the thruster exit than to the MN throat.

The (total) thrust can be split into

$$F = F_p + F_f + F_m, \tag{31}$$

with F_p the pressure force at the back wall, F_f the friction force at the lateral wall due to impact and accommodation of heavy particles (most of them ions recombining into neutrals), and $F_m = \int_{\Omega_p} -j_\theta B_r d\Omega$ the magnetic thrust. Table 3 shows these contributions for the above magnetic configurations.

From the case $z_t = -6$cm to the case $z_t = 0$cm: F_p decreases slightly, F_m decreases much, as expected, due the contribution of the MN convergent side; and $-F_f$ decreases much. The friction force per unit of area F_f'' is plotted in Fig. 6 (d) for the 3 configurations: F_f'' is positive in the upstream side of the lateral wall, because of the ion backflow, and is negative in the downstream side of the that wall. In this last side, $-F_f''$ is the largest for $z_t = -6$cm due to the worst confinement of magnetic lines for this case. Overall, F does not change much between the 3 cases, although a maximum is found for the intermediate (nominal) case. For this one, the magnetic thrust contribution is only a 19%, while it increases to 44% for $z_t = -6$cm and becomes negative for $z_t = 0$cm. Further details on the magnetic thrust, given in Table 3, are obtained from the splitting in different regions

$$F_m = F_{m,s} + F_{m,p} = F_{m,c} + F_{m,d}, \tag{32}$$

with $F_{m,s}$ and $F_{m,p}$ corresponding to, respectively, the source and plume regions, and $F_{m,c}$ and $F_{m,d}$ to the divergent and convergent MN regions.

The results for the magnetic thrust differ from those of Ahedo-Navarro's simpler model [15], in which the radial magnetic field inside the source was set null, thus eliminating totally the negative contribution of the convergent MN. In the 3 configurations here, the radial component inside the source is below 5% of the total magnetic field. This small component is not enough to change much the maps of the main plasma magnitudes (densities, currents, electric potential...), and explains the near invariability of the sonic surface; but enough to create an important source magnetic force, positive or negative depending on the MN throat location. Furthermore, the friction force at the lateral wall is also very affected by the details of the magnetic topology. The sensitivity of the thrust contributions against the magnetic configuration are reported in experiments too [12, 50].

4 Further insights on the plasma response

4.1 On the electron anomalous cross-field transport

In the simulations here, the anomalous cross-field transport parameter is modeled as constant in the whole domain, since specific data from experiments, necessary for more sophisticated treatments, are not available yet. The sensitivity of the solution to this parameter, and the selection of the nominal value $\alpha_{ano} = 0.02$ are discussed briefly.

Figures 7 (a)-(b) illustrates the plasma-wall magnitudes for the cases of $\alpha_{ano} = 0.02$ and 0.01. With the reduction of the anomalous transport, there is a better magnetic confinement of the lateral wall, but also a better heating of the electrons, i.e. higher T_e, which increase the plasma losses at the unshielded back wall. Panel (a) shows the ion current to the wall, and panel (b) the average impact energies of ions and electrons. For $\alpha_{ano} = 0.01$, the ion recombination to the lateral wall decreases by 2-3 times, and the average impact energy of ions and electrons increase by similar factors. Table 2 illustrates the performances. The power losses to the walls (P_{wall}/P_a) are even a bit larger. Still, the lower wall recombination implies a higher production efficiency, and significantly reduces the power losses in inelastic collisions (P_{inel}/P_a) being η_{ene} higher. Overall, the thrust efficiency increases from $\eta_F = 9.7\%$ to 14.4%.

Simulations for more values of α_{ano} have been carried out as well, as shown in Fig. 7 (c) for the thrust efficiency. The anomalous transport becomes negligible (compared with the classical one) for $\alpha_{ano} \leq O(\nu_e/\omega_{ce} \sim 10^{-3})$, with typical values of ν_e about 10^6-$10^7 s^{-1}$ and ω_{ce} about 10^9-$10^{10} s^{-1}$. The thrust efficiency varies strongly, with η_F increasing from 3% for $\alpha_{ano} = 0.1$ to 18% for $\alpha_{ano} \leq O(10^{-3})$. The curve of $\eta_F(\alpha_{ano})$, as also shown in Fig. 7 (c), is related to the one of $\eta_{prod}(\alpha_{ano})$, and thus to the confinement of the lateral wall. (Indeed, the case $\alpha_{ano} \leq O(10^{-3})$ agrees well with the estimations of Ahedo-Navarro's model [15], in which the anomalous transport was not considered.) The strong variation of $\eta_F(\alpha_{ano})$ poses the problem of the selection for α_{ano} to fit with experimental data. The fitting of the electron temperature seems a good choice, since it is also much affected by α_{ano}: the average source T_e is 5, 10.2, 16.2 and 68.4eV, for $\alpha_{ano} = 0.1$, 0.02, 0.01 and 0.001, respectively. The values of α_{ano}, near the nominal one, lead to values of T_e typically measured for EPTs [7, 47].

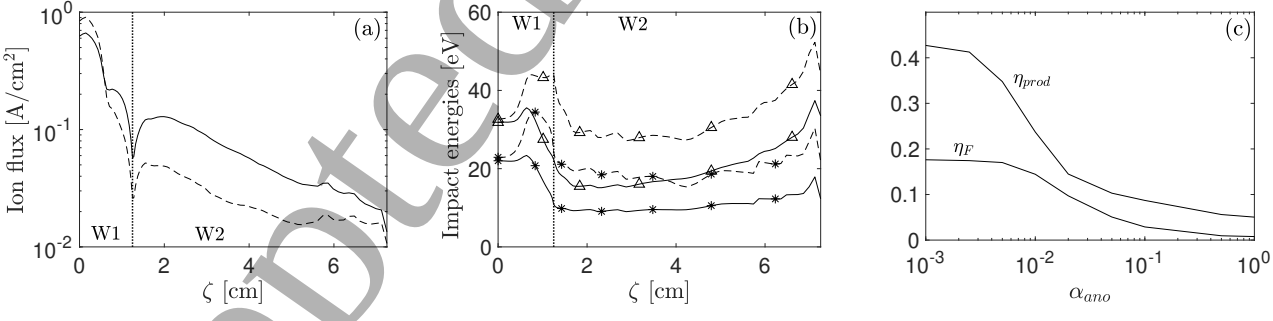

Figure 7: (a) Ion current density, (b) and mean impact energy of ions (△) and electrons (∗) to the thruster walls W1 and W2 (separated with a vertical dot line) for $\alpha_{ano} = 0.02$ (——) and $\alpha_{ano} = 0.01$ (- - - -). (c) Thrust and production efficiencies versus α_{ano}.

4.2 On the electron anomalous parallel cooling

In the nominal simulation, the effective collision frequency for the parallel thermal transport, ν_e' in Eq. (18), is used with $\nu_q = 10^9 s^{-1}$. The anomalous term dominates the cooling, typical values of ν_e are 10^6-$10^7 s^{-1}$, and would model the collisionless cooling (kinetic in nature) of electrons in expanding plumes.

An estimation, based on Eq. (18), of the value of ν_e' required to cool the electrons along the magnetic field lines in a plume of typical length L_p yields $\nu_e' \sim T_e/m_e L_p u_e \sim 10^9$-$10^{10}\text{s}^{-1}$, for L_p of few centimeters.

Figure 8 (a)-(b) illustrates these trends on T_e. Panel (a) shows the 2D map of T_e for $\nu_q = 0$, which is compared with Fig. 4 (c). Without the anomalous cooling, T_e is practically constant along the magnetic lines; distances of 1-10 meters would be needed to appreciate the cooling, which does not fit with experimental evidences. Panel (b) shows the 1D profiles of T_e for several ν_q along a magnetic line (panel (a), red line). As ν_q increases, the gradient of T_e is larger, and the peak T_e is also larger (similar total energy in the whole domain for the different cases); the effects are observable for $\nu_q \geq O(10^8\text{s}^{-1})$.

Figure 8 (c) shows T_e versus n_e in logarithmic scale along the plume part of the magnetic line. Many experimental [28, 29] and kinetic studies [33] indicate that a polytropic relation,

$$\gamma = 1 + \frac{\ln T_e/T_{e0}}{\ln n_e/n_{e0}}, \tag{33}$$

with γ a fitted polytropic coefficient (T_{e0} and n_{e0} refer to the thruster exit), approaches well measurements in the plume. The common values found in these studies are $\gamma = 1.15$-1.25 and the solution here for the nominal case with $\nu_q = 10^9\text{s}^{-1}$ fits well within this interval. For $\nu_q = 10^8\text{s}^{-1}$, γ is close to 1 and for $\nu_q = 10^{10}\text{s}^{-1}$ is about 1.4. Both the introduction of the anomalous parallel collisionality ν_q in the conductive Fourier's law or the use of a polytropic equation of state (instead of the energy equation) must be taken as phenomenological models, substituting consistent kinetic approaches to the phenomenon.

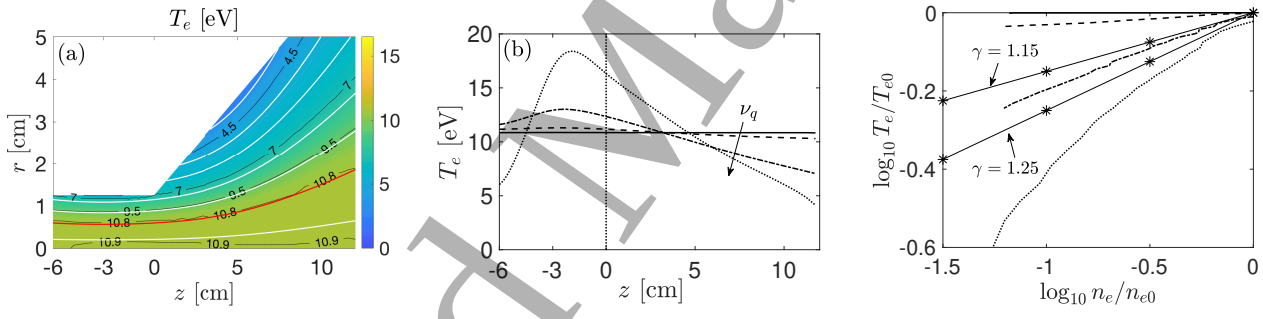

Figure 8: Results of T_e varying ν_q. (a) 2D map for $\nu_q = 0$. 1D profiles versus (b) z, and (c) versus n_e along a magnetic field line (red in (a)) for $\nu_q = 0$ (——), 10^8 (- - - -), 10^9 (-.-.-.-) and 10^{10}s^{-1} (. . . .). Polytropic curves ($*$) are shown in (c) for $\gamma = 1.15$ and 1.25 (results from experiments and kinetic studies are commonly between these two values).

4.3 On the effect of the plume extension

In the nominal simulation, the plume extension is not enough for a complete beam expansion. To assess the effect of the plume extension, a simulation is run with a double size of the plume, $L_p = 24$cm and $R_p = 10$cm, keeping the rest of parameters identical. The simulations assert that (i) plasma maps are practically identical in the common domain and (ii) the plume continues to expand in the additional domain. Figure 9 (a) shows these results with the 1D profiles of T_e along the red magnetic line of Fig. 8 (a). In the extended plume region, T_e continues to decay almost linearly with length from $\sim$ 7eV to $\sim$ 3eV (and ϕ decays additionally about 10V). Table 2 summarizes the effect of the additional expansion on the performances. The energy efficiency, η_{ene}, a source-related efficiency, remains the same. On the contrary, η_{div} and η_{disp}, which are plume-related efficiencies, increase 9-11% as the electron contribution to them decreases and the ion beam details dominate. The consequence is that thrust efficiency, η_F, increases from 9.7% to 12.3%. (Similar tendencies are observed in the table, for a given plume size, and

increasing ν_q for higher cooling rates.) Thus, simulations with a finite plume underestimate the total thrust. In fact, considering only the heavy species to compute η_{div} and η_{disp}, the values for the small and large plumes are nearly identical and equal to 91% and 89%, respectively. Taking these values as the final ones, once electrons are expanded completely, the thrust efficiency for an infinite plume is estimated as $\eta_F = 14.4\%$.

One more aspect we have analyzed is the value of c_q for the plume boundary condition on q_{ne}, Eq. (23). The specific value of c_q is not noticeable for very large plumes, since, irrespective of that value, electrons cool down and we have $q_{ne} = 0$ for an infinite plume. However, simulating very large plumes is expensive computationally, and selecting a proper value of c_q for a finite plume is important. Figure 9 (b) shows the 1D temperature profiles for $c_q = 0$ and 4, which, contrary to the nominal case $c_q = 2$ of Fig. 9(a), do not match for small and large plumes.

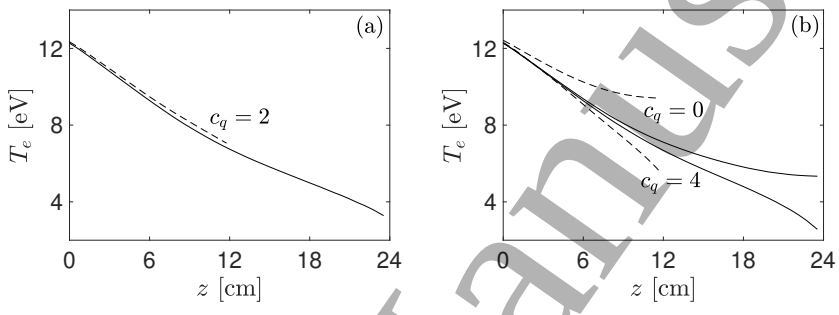

Figure 9: (a) 1D profile of T_e versus z along the red magnetic line of Fig. 8 (a) for $c_q = 2$, and (b) for $c_q = 0$ and $c_q = 4$.

4.4 On the effect of the power deposition map

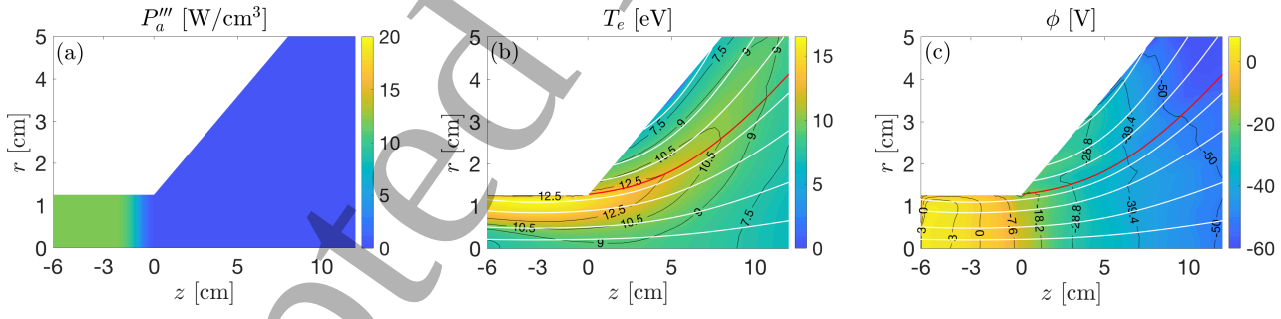

Figure 10: Results for (a) an uniform source power deposition map of (b) T_e and (c) ϕ.

The mechanisms of heating via the plasma-wave interaction are not the same for different types of EPT. In ECRTs, the heating is localized in the electron cyclotron resonance surface, while in HPTs, the power deposition is more spread with a device dependent pattern. In the nominal simulation, a Gaussian power deposition map is assumed, Fig. 3 (c). To evaluate the sensitivity of the plasma response to the deposition map, a simulation is run with the same P_a but a more uniform distribution for P_a''', as plotted in Fig. 10 (a). Since the total deposited power is the same, the peak of P_a''' is about 6 times lower. Fig. 10 (b) shows the 2D map of T_e, which is compared with Fig. 4 (c). Inside the source, the electron temperature is similar, about 9-16eV, but the profile is more uniform axially, and, radially, peaks off the axis (although P_a''' is uniform radially, the net power deposited locally scales with rP_a'''). In the plume, the profile of

cooling is similar. Fig. 10 (c) shows ϕ, and the comparison with Fig. 4 (d) is as proof that the differences in most plasma profiles are mild. Regarding the performances, the differences in the overall and partial efficiencies between the two cases are small (about 5% in relative terms).

5 Conclusions

A 2D axisymmetric fluid model of weakly-collisional, magnetized electrons is derived and then coupled with a PIC model for heavy species to analyze the plasma transport in electrodeless plasma thrusters. The numerical treatment of electron equations on a MFAM is complex. The algorithms proposed in Ref. [27] for the electric potential and current density equations is extended here to the temperature and energy flux equations. In addition, a linear, semi-implicit time scheme of the energy equation is implemented and shown to be convergence-robust.

The EPT discharge physics and performances, and the sensitivity to phenomenological parameters for anomalous cross-field transport and cooling are analyzed. Fluxes of particle and energy are rather aligned with magnetic lines in the main plasma plume but not inside the source. The current-free discharge does not satisfy local current ambipolarity, which implies that a full 2D model of the electron flows is necessary for a consistent description of currents.

The anomalous cross-field transport (likely due to turbulence, but little known in EPTs) implies large deterioration of the lateral wall magnetic confinement, leading to large power losses and ultimately in poor thrust efficiency, which is also penalized by the large losses in the unshielded back wall. This anomalous cross-field transport is tuned based on its correlation with the average source electron temperature. In addition, the anomalous parallel cooling is included to reproduce the experimentally observed plume cooling in EPTs (likely due to its collisionless, non-Maxwellian character). Interestingly, although the behavior of the electron energy model is not polytropic, it is shown that the profiles of electron density and temperature could be fitted approximately with a simple polytropic law.

The analysis of performances concludes clearly that the poor thrust efficiency of EPTs is due to the large wall and ionization losses inside the thruster vessel, which are caused by multiple re-ionization of wall-recombined neutrals. Magnetic shielding of the back wall, more magnetization (to compensate anomalous cross-field transport), and reduction of the vessel length will likely mitigate the losses, but they could have other penalties to be assessed.

The quasiaxial magnetic topology considered here includes a small radial magnetic field inside the vessel, which leads to negative magnetic thrust upstream of the MN throat. This is rather large (due to the large azimuthal plasma currents), for the case the throat is placed at the exit of the EPT (as it is common in HPTs). However, the small radial component has little effect on the ion transport and, thus, the location of the ion sonic surface is uncoupled with the location of the throat.

Since the slow decay of the magnetic field, the size of the simulated plasma plume influences the obtained plasma/thruster performances. The incomplete electron expansion (and demagnetization) tends to underestimates the thrust and the thrust efficiency. The computation of momentum and energy flows based on heavy species only seem a valid estimation for the infinite plume.

Currently, work in progress is attempting to couple consistently the plasma-wave model to the present plasma transport model. Nonetheless, the power deposition map is found here to have a mild effect on the global plasma transport. Further work will try to better tune anomalous transport and cooling expressions to experimental results on the plasma discharge (unavailable to us yet), until ultimately, physically-consistent anomalous models are derived and checked.

Acknowledgments

This research received initial funding from Airbus Defense and Space, contract number CW240050, and was completed thanks to funding from the HIPATIA project of HORIZON 2020 (European Commission), grant number GA870542.

A The sheath module

The S-module relates plasma magnitudes between the quasineutral edge Q and the wall W. For that, the model from Ref. [51] is implemented, which can be applied if the sheath is collisionless and unmagnetized. Here, the EPT plasma conditions are within these limits; indeed, taking the nominal simulation, we have that the Debye length, $\sqrt{\epsilon_0 T_e/e^2 n_e} \sim 10^{-3}$cm, is much smaller compared with the mean free path, $u_e/\nu_e \sim 10^{-1}$cm, and Larmor radius, $m_e\sqrt{T_e/m_e}/eB \sim 10^{-2}$cm.

In the simulated EPT, all walls are assumed made of ceramic material. This means significant secondary electron emission, and the current of electrons across the sheath is expressed as

$$j_{ne} = j_{np}(1-\delta_{wr})(1-\delta_{ws}), \tag{A.1}$$

where j_{np} is the current of primary electrons *to* the wall, and the secondary electron emission yields are modeled as

$$\delta_{wr}(T_{eQ}) = \delta_{r0}\frac{E_r^2}{(T_{eQ}+E_r)^2}, \quad \delta_{ws}(T_{eQ}) = \frac{2T_{eQ}}{E_s}, \tag{A.2}$$

and distinguish between the (true) secondary electrons emitted *from* the wall (δ_{ws}) with a temperature $T_s(\sim$1-2eV), and the elastically reflected primary electrons (δ_{wr}). The yields are dependent on the local temperature T_{eQ}, defined at the sheath edge Q. The parameters in the secondary yields δ_{r0}, E_r and E_s are dependent on the material, and for Boron-Nitride, we are taking $\delta_{r0} = 0.4$, $E_r = 20$eV and $E_s = 50$eV, and $T_s = 2$eV [51, 52].

In addition, the current of primary electrons is assumed to correspond to a near Maxwellian one with a replenishment level $\sigma_{rp}(\leq 1)$ (we take $\sigma_{rp} = 0.1$) for the high-energy tail of wall-collected electrons

$$j_{np}(\phi_{WQ}) = -e\sigma_{rp}n_{eQ}\frac{\bar{c}_{eQ}}{4}\exp\left(-\frac{e\phi_{WQ}}{T_{eQ}}\right), \tag{A.3}$$

with $\bar{c}_{eQ} = \sqrt{8T_{eQ}/\pi m_e}$ and ϕ_{WQ} the sheath potential drop.

The null net current condition at the dielectric wall means

$$j_{ne} = -j_{ni}, \tag{A.4}$$

and requires a potential drop satisfying

$$\frac{e\phi_{WQ}}{T_{eQ}} = \ln\left[\frac{en_{eQ}\bar{c}_{eQ}}{4j_{ni}}\sigma_{rp}\left(1-\delta_{wr}\right)\left(1-\delta_{ws}\right)\right]. \tag{A.5}$$

The flux of electron energy to the wall can be expressed as

$$P''_{neW} = \frac{2T_{eQ} - 2T_s\delta_{ws}}{(1-\delta_{ws})e}j_{ni}, \tag{A.6}$$

and the one to the sheath edge Q from the quasinuetral domain is

$$\frac{5T_{eQ}}{2e}j_{ni} + q_{neQ} = P''_{neW} + \phi_{WQ}j_{ni}, \tag{A.7}$$

which allows to obtain the boundary condition, needed in the E-module, for q_{neQ}.

B Numerical treatment of electron equations

The time discretization chosen for the electron equations yields

$$\nabla \cdot \boldsymbol{j}_e^{(k+1)} = -\nabla \cdot \boldsymbol{j}_i, \tag{B.1}$$

$$j_{pe}^{(k+1)} = \sigma_{pe}(T_e^{(k)}) \left[\frac{T_e^{(k)}}{e} \frac{\partial \ln n_e}{\partial \mathbf{1}_p} + \frac{1}{e} \frac{\partial T_e^{(k)}}{\partial \mathbf{1}_p} - \frac{\partial \phi^{(k+1)}}{\partial \mathbf{1}_p} \right] - j'_{pc}, \tag{B.2}$$

$$\nabla \cdot \boldsymbol{P}''^{(k+1)}_{\star e} = -\frac{3}{2} n_e \frac{T_e^{(k+1)} - T_e^{(k)}}{\Delta t_e} - \frac{3}{2} \frac{\partial n_e}{\partial t} T_e^{(k+1)} - \phi^{(k)} \nabla \cdot \boldsymbol{j}_i + P'''_a - P'''_{inel}(T_e^{(k)}), \tag{B.3}$$

$$P''^{(k+1)}_{\star pe} = -K_{pe}(T_e^{(k)}) \frac{\partial T_e^{(k+1)}}{\partial \mathbf{1}_p} + j_{pe}^{(k)} \left[\phi^{(k)} - \frac{5}{2} \frac{T_e^{(k+1)}}{e} \right], \tag{B.4}$$

where $p = \|, \perp$, and $(j'_{\|c}, j'_{\perp c}) = (j_{\|c}, (j_{\perp c} - \chi_t j_{\theta c})/(1 + \chi\chi_t))$. The current and energy systems are solved sequentially in time from step (k) to $(k+1)$ with a time step Δt_e: given T_e at (k), Eqs. (B.1)-(B.2) solve for ϕ and $\boldsymbol{j}_e$ at $(k+1)$; and given ϕ and $\boldsymbol{j}_e$ at (k), Eqs. (B.3)-(B.4) solve for T_e and $\boldsymbol{P}''_{\star e}$ at $(k+1)$.

The system of energy is the one with the temporal evolution character and the system of current follow this evolution, since both systems are coupled. The energy equation has the form $\partial T_e/\partial t = f(T_e, \nabla T_e)$, and a semi-implicit treatment is applied for $f(T_e, \nabla T_e)$: T_e is taken implicit (at step $(k+1)$) except in non-liner terms, for which T_e is taken explicit (at step (k)). This treatment is robust against Δt_e and at the same time keeps the numerical equations to be solved linear. Figure B.1 illustrates, for the nominal simulation, the temporal evolution of T_e and ϕ at the point $(z, r) = (0, 0.625)$cm versus the number of subiterations N_e ($\Delta t_e = \Delta t/N_e$, and $\Delta t = 2.5 \cdot 10^{-8}$). (The explicit treatment of $f(T_e, \nabla T_e)$ would be much simpler, but strong limit exist for Δt_e [53]; just as illustration, for the nominal simulation, the limit is $\Delta t < 10^{-12}$s, and the minimum number of subiterations inside the E-module would be $N_e \sim 10^4$.)

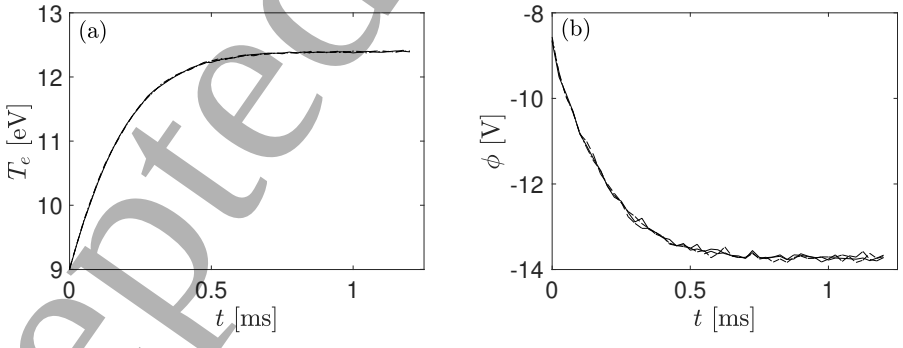

Figure B.1: Temporal evolution of (a) T_e, and (b) ϕ at the point $(z, r) = (0, 0.625)$cm obtained with the semi-implicit scheme for $N_e = 1$ (-.-.-.-.), 5 (- - - -) and 10 (——).

The spatial discretization of the above equations is done in a MFAM with the numerical algorithms developed in Ref. [27] for Eqs. (B.1)-(B.2), and $(\phi, \boldsymbol{j}_e)$. Since Eqs. (B.3)-(B.4) for $(T_e, \boldsymbol{P}''_{\star e})$ present the same functional form, the same numerical algorithms are valid. A finite volume method (FVM) is used for the conservation law (current or energy), and a gradient reconstruction method (GRM) for the corresponding property flux.

The conservation laws (B.1) and (B.3) can be written in a generic way as $\nabla \cdot \mathbf{\Gamma} = S$, with $\mathbf{\Gamma}$ a flux ($\boldsymbol{j}_e$ or $\boldsymbol{P}''_{\star e}$), and S a source term. Applying the FVM for a cell yields

$$\sum_m A_m \Gamma_{nm} = S_l \Omega_l, \qquad \Gamma_{nm} = \mathbf{\Gamma} \cdot \boldsymbol{n}_m, \tag{B.5}$$

where: index l denotes the cell and Ω_l is its volume; index m denotes a face of the cell, A_m is its area and $\boldsymbol{n}_m$ is its outwards normal. The source term is evaluated at the cell centers, and the fluxes are evaluated at the face centers. For non-boundary faces Γ_{nm} is either $\pm\Gamma_\parallel$ or $\pm\Gamma_\perp$, and for the boundary faces Γ_{nm} comes from the boundary condition. These fluxes are related to the gradient of a scalar ψ (ϕ or T_e) as $\Gamma_p = -k_p \partial\psi/\partial \mathbf{1}_p + \Gamma'_p$, with k_p a conductivity and Γ'_p an additional term. The derivatives are discretized with a GRM as

$$\left.\frac{\partial \psi}{\partial \mathbf{1}_p}\right|_m = \sum_l g_{p,ml} \psi_l, \tag{B.6}$$

where $g_{p,ml}$ are geometric coefficients, for direction p, of the face m with respect to the cells l. For the computation of the numerical derivatives, i.e. $g_{p,ml}$, a stencil of the surrounding cells is needed, which depends on the particular GRM [27]. A FDM is applied for the faces of inner cells, which are structured in the magnetic frame and allow these methods. For the faces of boundary cells, which are unstructured, a WLSM is applied instead. These methods are versatile, independent of the cells layout, but are prone to producing numerical diffusion since derivatives along different directions are computed at the same time. Furthermore, the fluxes can be also related to ψ itself, via Γ'_p. The value of ψ at the face m is obtained as

$$\psi_m = \sum_l g_{ml} \psi_l, \tag{B.7}$$

and an linear interpolation method is used to compute the coefficients g_{ml}.

Applying Eq. (B.5) to all the cells yields the matrix system

$$A_1\{\Gamma_{nm^*}\} + A'_1\{\psi_l\} = B_1, \tag{B.8}$$

where: A_1 is a matrix for the areas of the cell faces; $\{\Gamma_{nm^*}\}$ is a vector grouping the values of Γ_{nm} at the non-boundary faces m^*; A'_1 is a matrix for the source term part dependent on ψ; $\{\psi\}$ is a vector of the values of ψ at the cells; and B_1 is a vector for the source term part independent of ψ, and the boundary conditions. Then, Eqs. (B.6)-(B.7) for the fluxes yield

$$\{\Gamma_{nm^*}\} = A_2\{\psi_l\} + B_2, \tag{B.9}$$

with A_2 containing the gradient reconstruction and interpolation coefficients; and B_2 containing the terms independent of ψ. Eliminating $\{\Gamma_{nm*}\}$ between the two last equations yields the matrix system for solving $\{\psi_l\}$,

$$A\{\psi_l\} = B, \tag{B.10}$$

with the matrix $A = A_1 A_2 + A'_1$ and the vector $B = B_1 - A_1 B_2$. This last system solve for inner magnitudes, and to complete the plasma solution in the whole domain, the boundary magnitudes are also needed. For the solution at boundary faces, a GRM based on a modified WLSM is used [27] for solving from the boundary conditions.

C Computation of species flows

In the PIC formulation of heavy species, the flows through the simulation domain surfaces are computed using surface weighting algorithms [24]. For a discrete surface panel and within a time step Δt, there are macroparticles p with weight N_p (i.e. number of elementary particles) of the species s crossing the surface with total velocity v_p and axial velocity v_{zp}. Then, the flows of mass, axial momentum, total and axial energy of species s across a single panel are, respectively,

$$\Delta\dot{m}_s = \frac{m_s}{\Delta t}\sum_p N_p, \quad \Delta\dot{M}_{zs} = \frac{m_s}{\Delta t}\sum_p N_p v_{zp}, \quad \Delta P_s = \frac{m_s}{\Delta t}\sum_p N_p \frac{v_p^2}{2}, \quad \Delta P_s^{(z)} = \frac{m_s}{\Delta t}\sum_p N_p \frac{v_{zp}^2}{2}. \tag{C.1}$$

Adding for all panels of a surface W, the flows across that surface are

$$\dot{m}_{s,W} = \sum_W \Delta\dot{m}_s, \quad \dot{M}_{zs,W} = \sum_W \Delta\dot{M}_{zs}, \quad P_{s,W} = \sum_W \Delta P_s, \quad P_{s,W}^{(z)} = \sum_W \Delta P_s^{(z)}. \tag{C.2}$$

In the fluid formulation of electrons ($s = e$), the same flows for the surface W are defined as

$$\begin{aligned}
\dot{m}_{s,W} &= \textstyle\int_W m_s n_s \boldsymbol{u}_s \cdot \boldsymbol{n} dS, \\
\dot{M}_{zs,W} &= \textstyle\int_W \mathbf{1}_z \cdot (m_s n_s \mathbf{u}_s \mathbf{u}_s + \bar{\bar{p}}_s) \cdot \mathbf{n} dS, \\
P_{s,W} &= \textstyle\int_W \left[\left(\frac{1}{2} m_s u_s^2 + \frac{1}{2}\operatorname{tr}(\bar{\bar{p}}_s)/n_s\right) n_s \boldsymbol{u}_s + \boldsymbol{u}_s \cdot \bar{\bar{p}}_s + \boldsymbol{q}_s \right] \cdot \boldsymbol{n} dS, \\
P_{s,W}^{(z)} &= \textstyle\int_W \left[\left(\frac{1}{2} m_s u_{zs}^2 + \frac{1}{2}\mathbf{1}_z \cdot \bar{\bar{p}}_s \cdot \mathbf{1}_z/n_s\right) n_s \boldsymbol{u}_s + u_{zs}\mathbf{1}_z \cdot \bar{\bar{p}}_s + \boldsymbol{q}_s^{(z)} \right] \cdot \boldsymbol{n} dS.
\end{aligned} \tag{C.3}$$

For the flows, the thermal terms are included being $\bar{\bar{p}}_s$ the pressure tensor, $\boldsymbol{q}_s$ and $\boldsymbol{q}_s^{(z)}$ the heat fluxes of, respectively, total and axial energy. In the isotropic-temperature model here, we have that $\bar{\bar{p}}_e = n_e T_e \bar{\bar{I}}$, and $\boldsymbol{q}_e^{(z)} = \boldsymbol{q}_e/3$.

Finally, the thrust is defined as the downstream free-loss surface $W3$ momentum flow

$$F = \sum_s \dot{M}_{zs,W3}. \tag{C.4}$$

Two related magnitudes of interest are the 'pressure force' at the back wall $W1$ and the 'friction force' at the lateral wall $W2$,

$$F_p = -\sum_s \dot{M}_{zs,W1}, \qquad F_f = -\sum_s \dot{M}_{zs,W2}. \tag{C.5}$$

References

[1] Mario Merino and Eduardo Ahedo. Magnetic nozzles for space plasma thrusters. In J. Leon Shohet, editor, *Encyclopedia of Plasma Technology*, volume 2, pages 1329–1351. Taylor and Francis, 2016.

[2] J.C. Sercel. *An experimental and theoretical study of the ECR plasma engine*. PhD thesis, California Institute of Technology, 1993.

[3] D. Packan, P.Q. Elias, J. Jarrige, M. Merino, A. Sánchez-Villar, E. Ahedo, G. Peyresoubes, K. Holste, P. Klar, M. Bekemans, T. Scalais, E. Bourguignon, S. Zurbach, M. Mares, A. Hooque, and P. Favier. The MINOTOR H2020 project for ECR thruster development. In 35^{th} *International Electric Propulsion Conference*, number IEPC-2017-547. Electric Rocket Propulsion Society, 2017.

[4] Kazunori Takahashi, Christine Charles, Rod Boswell, and Akira Ando. Performance improvement of a permanent magnet helicon plasma thruster. *Journal of Physics D: Applied Physics*, 46(35):352001, 2013.

[5] Shunjiro Shinohara, Hiroyuki Nishida, Takao Tanikawa, Tohru Hada, Ikkoh Funaki, and Konstantin P Shamrai. Development of electrodeless plasma thrusters with high-density helicon plasma sources. *IEEE Transactions on Plasma Science*, 42(5):1245–1254, 2014.

[6] E. Toson, D. Moretto, M. Magarotto, and et al. Development and testing of a miniature helicon plasma thruster. In *35th International Electric Propulsion Conference, Atlanta, GA, IEPC-2017-519*, 2017.

[7] J Navarro-Cavallé, M Wijnen, P Fajardo, and E Ahedo. Experimental characterization of a 1 kw helicon plasma thruster. *Vacuum*, 149:69–73, 2018.

[8] Mario Merino and Eduardo Ahedo. Contactless steering of a plasma jet with a 3D magnetic nozzle. *Plasma Sources Science and Technology*, 26(9):095001, 2017. doi:10.1088/1361-6595/aa8061.

[9] R. Imai and K. Takahashi. Demonstrating a magnetic steering of the thrust imparted by the magnetic nozzle radiofrequency plasma thruster. *Applied Physics Letters*, 118:264102, 2021.

[10] T. Vialis, J. Jarrige, A. Aanesland, and D. Packan. Direct thrust measurement of an electron cyclotron resonance plasma thruster. *Journal of Propulsion and Power*, 34(5):1323–1333, 2018.

[11] M. Umair Siddiqui, C. Cretel, J. Synowiec, Andrea G. Hsu, Jason A. Young, and R. Spektor. First performance measurements of the phase four rf thruster. In *35th International Electric Propulsion Conference, Atlanta, GA.*, IEPC-2017-431, 2017.

[12] K. Takahashi and A. Ando. Enhancement of axial momentum lost to the radial wall by the upstream magnetic field in a helicon source. *Plasma Physics and Controlled Fusion*, 59:054007, 2017.

[13] A. Fruchtman, G. Makrinich, and J. Ashkenazy. Two-dimensional equilibrium of a low temperature magnetized plasma. *Plasma Sources Science and Technology*, 14:152–167, 2005.

[14] E. Ahedo, J.M. Gallardo, and M. Martínez-Sánchez. Effects of the radial-plasma wall interaction on the axial Hall thruster discharge. *Physics of Plasmas*, 10(8):3397–3409, 2003.

[15] Eduardo Ahedo and Jaume Navarro-Cavallé. Helicon thruster plasma modeling: Two-dimensional fluid-dynamics and propulsive performances. *Physics of Plasmas*, 20(4):043512, 2013.

[16] Eduardo Ahedo and Mario Merino. Two-dimensional supersonic plasma acceleration in a magnetic nozzle. *Physics of Plasmas*, 17(7):073501, 2010.

[17] J. M. Fife. *Hybrid-PIC modeling and electrostatic probe survey of Hall thrusters*. PhD thesis, Massachusetts Institute of Technology, 1998.

[18] F. I. Parra, E. Ahedo, J. M. Fife, and M. Martínez-Sánchez. A two-dimensional hybrid model of the Hall thruster discharge. *Journal of Applied Physics*, 100(2):023304, 2006.

[19] E. Choueiri. Plasma oscillations in Hall thrusters. *Physics of Plasmas*, 8(4):1411–1426, 2001.

[20] J. Cavalier, N. Lemoine, G. Bonhomme, S. Tsikata, C. Honoré, and D. Grésillon. Hall thruster plasma fluctuations identified as the e×b electron drift instability: Modeling and fitting on experimental data. *PoP*, 20(8):082107, 2013.

[21] J.P. Boeuf. Tutorial: Physics and modeling of Hall thrusters. *J. Applied Physics*, 121(1):011101, 2017.

[22] Shadrach Hepner, Benjamin Wachs, and Benjamin Jorns. Wave-driven non-classical electron transport in a low temperature magnetically expanding plasma. *Applied Physics Letters*, 116(26):263502, 2020. doi:10.1063/5.0012668.

[23] Daniel Pérez-Grande. *Fluid modeling and simulation of the electron population in Hall effect thrusters with complex magnetic topologies*. PhD thesis, Universidad Carlos III de Madrid, Leganés, Spain, 2018.

[24] Adrián Domínguez-Vázquez. *Axisymmetric simulation codes for Hall effect thrusters and plasma plumes*. PhD thesis, Universidad Carlos III de Madrid, Leganés, Spain, 2019.

[25] Jiewei Zhou. *Modeling and simulation of the plasma discharge in a radiofrequency thruster*. PhD thesis, Universidad Carlos III de Madrid, Leganés, Spain, 2021.

[26] I.G. Mikellides and I. Katz. Numerical simulations of hall-effect plasma accelerators on a magnetic-field-aligned mesh. *Physical Review E*, 86(4):046703, 2012.

[27] Jiewei Zhou, Daniel Pérez-Grande, Pablo Fajardo, and Eduardo Ahedo. Numerical treatment of a magnetized electron fluid within an electromagnetic plasma thruster code. *Plasma Sources Science and Technology*, 28(11):115004, 2019.

[28] JM Little and EY Choueiri. Electron cooling in a magnetically expanding plasma. *Physical Review Letters*, 117(22):225003, 2016.

[29] Yunchao Zhang, Christine Charles, and Rod Boswell. Thermodynamic study on plasma expansion along a divergent magnetic field. *Physical review letters*, 116(2):025001, 2016.

[30] June Young Kim, KS Chung, Seongcheol Kim, Jong Hyeon Ryu, Kyoung-Jae Chung, and YS Hwang. Thermodynamics of a magnetically expanding plasma with isothermally behaving confined electrons. *New Journal of Physics*, 20(6):063033, 2018.

[31] T.A. Collard and B.A. Jorns. Magnetic nozzle efficiency in a low power inductive plasma source. *Plasma Sources Science and Technology*, 28:105019, 2019.

[32] Eduardo Ahedo, Sara Correyero, Jaume Navarro, and Mario Merino. Macroscopic and parametric study of a kinetic plasma expansion in a paraxial magnetic nozzle. *Plasma Sources Science and Technology*, 29(4):045017, 2020. doi:10.1088/1361-6595/ab7855.

[33] Jiewei Zhou, Gonzalo Sánchez-Arriaga, and Eduardo Ahedo. Time-dependent expansion of a weakly-collisional plasma beam in a paraxial magnetic nozzle. *Plasma Sources Science and Technology*, 30(4):045009, 2021. doi:10.1088/1361-6595/abeff3.

[34] E. Zawaideh, N.S. Kim, and F. Najmabadi. Generalized parallel heat transport equations in collisional to weakly collisional plasmas. *The Physics of Fluids*, 31:3280–3285, 1988.

[35] Bin Tian, Mario Merino, and Eduardo Ahedo. Two-dimensional plasma-wave interaction in an helicon plasma thruster with magnetic nozzle. *Plasma Sources Science and Technology*, 27(11):114003, 2018.

[36] A. Sánchez-Villar, J. Zhou, M. Merino, and E. Ahedo. Coupled plasma transport and electromagnetic wave simulation of an ECR thruster. *Plasma Sources Science and Technology*, 30(4):045005, 2021. doi:10.1088/1361-6595/abde20.

[37] Daniel Pérez-Grande, O. González-Martínez, Pablo Fajardo, and Eduardo Ahedo. Analysis of the numerical diffusion in anisotropic mediums: benchmarks for magnetic field aligned meshes in space propulsion simulations. *Applied Sciences*, 6(11):354, 2016.

[38] Filippo Cichocki, Adrián Domínguez-Vázquez, Mario Merino, and Eduardo Ahedo. Hybrid 3D model for the interaction of plasma thruster plumes with nearby objects. *Plasma Sources Science and Technology*, 26(12):125008, 2017.

[39] Adrián Domínguez-Vázquez, Filippo Cichocki, Mario Merino, Pablo Fajardo, and Eduardo Ahedo. Axisymmetric plasma plume characterization with 2D and 3D particle codes. *Plasma Sources Science and Technology*, 27(10):104009, 2018. doi:10.1088/1361-6595/aae702.

[40] Stephen Francis Biagi. Cross sections extracted from PROGRAM MAGBOLTZ, version 7.1 june 2004, June 2004. [Online; accessed 5-July-2021]. URL: www.lxcat.net/Biagi-v7.1.

[41] M. Mitchner and C.H. Kruger Jr. *Partially ionized gases*. John Wiley and Sons, Hoboken, NJ, 1973.

[42] S Correyero, J Jarrige, D Packan, and E Ahedo. Plasma beam characterization along the magnetic nozzle of an ECR thruster. *Plasma Sources Science and Technology*, 28(9):095004, 2019. doi:10.1088/1361-6595/ab38e1.

[43] C. Charles, R.W. Boswell, and K. Takahashi. Boltzmann expansion in a radiofrequency conical helicon thruster operating in xenon and argon. *Applied Physics Letters*, 102:223510, 2013.

[44] E. Ahedo. Parametric analysis of a magnetized cylindrical plasma. *Physics of Plasmas*, 16(11):113503, 2009.

[45] Mario Merino and Eduardo Ahedo. Plasma detachment in a propulsive magnetic nozzle via ion demagnetization. *Plasma Sources Science and Technology*, 23(3):032001, 2014. doi:10.1088/0963-0252/23/3/032001.

[46] Eduardo Ahedo and Mario Merino. Two-dimensional plasma expansion in a magnetic nozzle: separation due to electron inertia. *Physics of Plasmas*, 19(8):083501, 2012.

[47] Kazunori Takahashi, Aiki Chiba, Atsushi Komuro, and Akira Ando. Experimental identification of an azimuthal current in a magnetic nozzle of a radiofrequency plasma thruster. *Plasma Sources Sci. Technol.*, 25(5):055011, August 2016. doi:10.1088/0963-0252/25/5/055011.

[48] Nathan P. Brown and Mitchell L. R. Walker. Review of plasma-induced hall thruster erosion review of plasma-induced hall thruster erosion. *Applied Sciences*, 10(11):3775, 2020.

[49] A Fruchtman, K Takahashi, C Charles, and RW Boswell. A magnetic nozzle calculation of the force on a plasma. *Physics of Plasmas (1994-present)*, 19(3):033507, 2012.

[50] K. Takahashi, T. Lafleur, C. Charles, P. Alexander, and R.W. Boswell. Electron diamagnetic effect on axial force in an expanding plasma: Experiments and theory. *Physical Review Letters*, 107(23):235001, 2011.

[51] E. Ahedo and V. de Pablo. Combined effects of electron partial thermalization and secondary emission in Hall thruster discharges. *Physics of Plasmas*, 14:083501, 2007.

[52] F. Taccogna, S. Longo, and M. Capitelli. Plasma sheaths in Hall discharge. *Physics of Plasmas*, 12(9):093506, 2005.

[53] G.J.M. Hagelaar and G.M.W. Kroesen. Speeding up fluid models for gas discharges by implicit treatment of the electron energy source term. *Journal of Computational Physics*, 159(1):1–12, 2000.